JYX
JYVÄSKYLÄN YLIOPISTO
UNIVERSITY OF JYVÄSKYLÄ

This is a self-archived version of an original article. This version may differ from the original in pagination and typographic details.

Author(s): Laine, Petteri; Välikangas, Juho; Kauppinen, Toni; Hu, Tao; Wang, Shubo; King, Graham; Singh, Harishchandra; Tynjälä, Pekka; Lassi, Ulla

Title: Synergistic effects of low-level magnesium and chromium doping on the electrochemical performance of LiNiO2 cathodes

Year: 2024

Version: Published version

Copyright: © 2023 the Authors

Rights: CC BY 4.0

Rights url: https://creativecommons.org/licenses/by/4.0/

Please cite the original version:

Laine, P., Välikangas, J., Kauppinen, T., Hu, T., Wang, S., King, G., Singh, H., Tynjälä, P., & Lassi, U. (2024). Synergistic effects of low-level magnesium and chromium doping on the electrochemical performance of LiNiO2 cathodes. Journal of Solid State Electrochemistry, 28(1), 85-101. https://doi.org/10.1007/s10008-023-05652-1

Journal of Solid State Electrochemistry
https://doi.org/10.1007/s10008-023-05652-1

ORIGINAL PAPER

Synergistic effects of low-level magnesium and chromium doping on the electrochemical performance of $LiNiO_2$ cathodes

Petteri Laine[1,2] · Juho Välikangas[1,2] · Toni Kauppinen[1,2] · Tao Hu[1] · Shubo Wang[3] · Graham King[4] · Harishchandra Singh[3] · Pekka Tynjälä[1,2] · Ulla Lassi[1,2]

Received: 18 June 2023 / Revised: 17 August 2023 / Accepted: 22 August 2023
© The Author(s) 2023

Abstract
$LiNiO_2$ cathode materials with magnesium and chromium doping were prepared using a simple low-cost and efficient co-precipitation and lithiation procedure. During this procedure, both magnesium and chromium form a concentrated core particle, unto which nickel hydroxide precipitates. During lithiation, the elements in question will redistribute themselves and form a homogenous mixture. Magnesium-containing materials exhibit an excellent electrochemical performance, due to phase stabilizing effects, while for chromium-containing materials, performance remains poor. Rietveld refinement reveals that there is a possible upper limit for Mg doping (~2.5 mol%) as a pilar dopant. Washing of the lithiated materials was explored, and it is proposed that this can improve capacity retention in prolonged cycling. However, the inevitable loss of lithium from the surface layer remains a challenge. Two sources for the chromium facilitated capacity decay are proposed, both owing to the highly irreversible redox reaction of hexavalent chromium possibly blocking lithium pathways.

Keywords $LiNiO_2$ · Cathode material · Magnesium and chromium doping · Co-precipitation · Cobalt free

Introduction

Global changes in policy toward sustainable mobility and the reduction of conventionally fueled vehicles due to global climate change [1] have driven the adoption of electric vehicles, and their numbers are estimated to increase tenfold by the year 2030 [2]. To meet this increase in the global demand for battery materials, novel battery chemistries that provide high performance at affordable costs are needed. To this effect, high nickel and low cobalt-containing cathode materials have emerged as future alternatives, due mainly to the high price of cobalt and potential global availability concerns [2]. Among these materials, $LiNiO_2$ (LNO), which is isostructural to the layered $LiCoO_2$, has garnered considerable interest due to its theoretically high capacity (274 mAh/g) and relatively low cost. There are, however, several issues that need to be resolved before pristine LNO can be successfully utilized in electric-vehicle applications, namely poor capacity retention, low thermal runaway temperature, and difficulties in the preparation of stoichiometrically pure material without cation mixing [3]. While it has been possible to prepare near-stoichiometrically pristine LNO materials [4], poor capacity retention originating from cycling induced microcracking of the primary particles at higher voltages [5], surface reactions with electrolytes, and oxygen evolution from the particle surface remain challenges [6].

Various strategies and techniques, among them elemental doping and coating, have been proposed to mitigate the aforesaid drawbacks of LNO and high nickel-containing cathode materials [7, 8]. Among the dopants employed, magnesium has been used to dope a wide array of nickel-containing cathode materials [3, 9–13]. The beneficial effects of magnesium doping are generally attributed to Mg^{2+} cations occupying Li^+ positions in the layered structure, as proposed by Delmas et al. [3] and Pouillerie et al. [9]. These electrochemically inert Mg^{2+} ions hinder the localized structural collapse caused by the oxidation

✉ Ulla Lassi
ulla.lassi@oulu.fi

1 Research Unit of Sustainable Chemistry, University of Oulu, P.O. Box 4000, FI-90014 Oulu, Finland

2 University of Jyvaskyla, Kokkola University Consortium Chydenius, Talonpojankatu 2B, FI-67100 Kokkola, Finland

3 Nano and Molecular Systems Research Unit (NANOMO), University of Oulu, FI-90014 Oulu, Finland

4 Canadian Light Source, 44 Innovation Blvd, Saskatoon, SK S7N 2V3, Canada

Published online: 06 September 2023

of divalent nickel, which, in turn, obstruct lithium diffusion in the layered structure. This research was further expanded to NCM (nickel–cobalt - manganese) materials by Li et al. [10] and Xie et al. [11], who further proposed that this "pillaring" effect will increase phase reversibility and thermal stability, leading to improved electrochemical performance, even if the Mg content is relatively low (2–3 mol %).

Additionally, magnesium has been used in conjunction with other dopants such as Al, Ti [14–16], Mn [17], and Cu [18] to further improve electrochemical properties. This binary doping strategy was further elaborated by Yosida et al. [19]. Researchers proposed, through density functional theory - based calculations, various dopant combinations, which would have synergistic effects on the positive performance of the cathode material. These effects would especially mitigate microcracking stemming from volumetric change, which was identified by the authors as the most significant issue causing reduced capacity retention. Among the most interesting material combinations, Cr - Re and Cr - Mg proved to reduce the volumetric change of the material most effectively. However, experimental validation supporting these findings is still insufficient.

Individually, chromium has been used to dope in high nickel - containing cathode materials and other layered materials [20, 21]. Mohan et al. [22] synthesized LNO nanoparticles containing various amounts of chromium through a sol–gel synthesis method. In comparison to pristine LNO, the synthesized materials showed an improved charge and discharge capacity, as well as improved capacity retention when chromium substitution was less than 10 mol %. These researchers suggest that chromium stabilizes the oxide layer structure and thus facilitates lithium diffusion in the structure. However, Li et al. [23] report a reduced electrochemical performance of NCM 811 cathode material even at relatively low chromium doping levels (3 mol %), while 1 mol % improved the performance. This was suggested as being partly the result of the appearance of Cr^{6+} and Mn^{3+} ions, which would enter the lithium layer and compromise the electrochemical performance by blocking lithium intercalation pathways.

The present work aims to study the low - level doping of LNO cathode material with magnesium and chromium prepared via a simple two - step co - precipitation and lithiation procedure. Precursor materials containing Mg and Cr individually or in combination will be co - precipitated as hydroxide precursors. These materials will then be lithiated, and their physicochemical and electrochemical properties will be analyzed and tested. Furthermore, the influence of washing and lithiation temperature on the cathode material properties will be explored.

Materials and methods

Preparation of the magnesium and chromium - doped $Ni(OH)_2$ precursors

All precipitation experiments were carried out in a 3 - L continuous stirred - tank reactor (CSTR) under inert conditions, to which three separate feeds of nickel sulfate, sodium hydroxide, and ammonia solutions were continuously fed under vigorous stirring at a temperature of 50 °C. The nickel - containing feed solutions were prepared by dissolving solid $NiSO_4 * 6H_2O$ in ion - exchanged water, in which the desired amounts of solid $MgSO_4 * 7H_2O$ and / or $CrCl_3 * 6H_2O$ were further dissolved to a combined total of 1.5 mol / L in the feed solution. A solution of 2.5 mol / L NaOH was prepared in a similar fashion. The reactor was preloaded with ammonia - water and heated to the desired temperature. During the experiment, feed rates were carefully monitored and controlled to achieve a residence time of approximately 4 h at the desired pH range. Particle size distribution, pH, and ammonia concentration were measured periodically throughout the experiment. After the desired particle size was reached (12–17 h), the reactor content was filtrated and washed thoroughly with ion - exchanged water. After filtration, the material was dried in a vacuum oven under nitrogen gas flow at 60 °C for 12 h.

The precipitated $Ni(OH)_2$ precursor materials and lithiated LNO materials prepared from those precursor materials are hereafter referred to as P - LNO - x and LNO - x, where prefix P is used for $Ni(OH)_2$ materials and a suffix x and a numbering system indicate the dopant material, i.e., Mg for magnesium and Cr for chromium and the amount of dopant in mol %. Furthermore, the lithiation temperature and time are indicated after the dopant concentration when necessary. Additionally, WD is used for washed samples.

Lithiation

The $Ni(OH)_2$ precursor was thoroughly mixed with excess LiOH and then lithiated. An LiOH excess was used to compensate for the lithium lost during high - temperature calcination and to ensure homogeneous lithiation. The mixtures were initially calcined at 670 °C for 5 h in an oxygen atmosphere with a 2.5 °C / min heating ramp. For magnesium - containing samples, additional experiments at temperatures of 650 °C, 670 °C and 690 °C were made, whereby lithiation time was increased to 10 h. After lithiation, the material was further milled and sieved to less than 40 µm in dry room conditions. After the milling and sieving procedures, samples were washed with deionized water and dried in vacuum oven at 180 °C.

Cell assembling and electrochemical characterization

Electrochemical performance testing was carried out in half-cells, with metallic lithium as the counter electrode and full cells with graphite as the anode material. All electrode foils and battery cells were prepared in dry-room conditions. The foil-making procedure, coin and pouch cell assembly, and testing procedures are described in detail by Välikangas et al. [4]. For coin cell testing, C-rates were calculated based on 200 mAh/g with active material loading on the foils between 11.58–13.06 mg/cm^2. For pouch cells, a C-rate of 250 mAh/g was used with active material loading on the foils between 10.42 and 11.48 mg/cm^2. Differential capacity measurements were made from the same coin cells as the other electrochemical measurements.

Characterization of samples

The tap density of the powders was measured using an Erweka SVM222 tap density device and following the ISO EN 787/11 standard. Residual lithium was measured with an automatic titrator. Particle size distribution (PSD) during precipitation was measured with a Malvern Mastersizer 3000.

Lab source X-ray diffraction (XRD) was measured with Rigaku SmartLab 9 kW X-ray diffractometers and using Co as a source at 40 kV, 135 mA. Diffractograms were collected in the 2θ range (5–120° at 0.01° intervals) with a scan speed of 4.06 deg/min. Peaks were identified using the database of the International Centre for Diffraction Data (PDF-4+2020). The crystallite sizes as well as anisotropy and distribution were computed using the Rikagu PDXL2 analysis package. Whole powder pattern fitting was used for the decomposition and least-square Pawley method. The peak shape was modeled using the fundamental parameter method with continuous scanning and the Cheary–Coelho axial model, using experimental geometry and optics. The crystallite shape was refined as an ellipsoidal shape, with a lognormal distribution used as the free parameter for iterative refinement other than spherical shape, which is a better fit for the crystal structure of LNO.

Synchrotron hard X-ray measurements of samples in the above section were carried out at the Brockhouse High Energy Wiggler Beamline, Canadian Light Source (CLS), Canada. A 2D Perkin Elmer detector, 200×200 μm^2 pixel size and 40×40 cm^2 in area, was placed downstream of the powders in a Kapton capillary, allowing data acquisition in a Debye–Scherrer/transmission mode. Synchrotron X-ray diffraction (SXRD) and total scattering patterns for pair distribution function (PDF) were acquired using a monochromatic focused beam of 65 keV. The calibrated X-ray wavelength and sample-to-detector from an Ni calibrant for XRD pattern acquisition were $\lambda = 0.2038$ Å and 918.3 mm, respectively. The representative-obtained 2D diffraction patterns were integrated in a radial direction by the GSAS-II software [24]. The resulting 1D SXRD profiles were then analyzed using Rietveld refinement analysis. Total scattering data for the atomic PDF were collected at a sample-to-detector distance of 158.8 mm. Total scattering data were transformed into PDF, G(r), by applying a $Q_{max} = 25$ Å^{-1}. An empty Kapton capillary was measured under identical conditions to subtract the container contribution from the PDFs.

The microstructures shown in the field-emission scanning electron microscopy (FESEM) images were obtained using a Zeiss Sigma FESEM operating at 5 kV. Both XRD and FESEM were performed at the Centre for Material Analysis of the University of Oulu. Composition of the solid samples were determined using ICP-OES (Agilent 5110 VDV ICP-OES). ICP-OES analysis was performed on the solid precipitates, and corresponding metal lithium and dopant ratios was confirmed. Microwave digestion was used for total dissolution of these samples without any leaching residue. This was carried out based on the EPA3051A standard using nitric acid: hydrochloric acid with the ratio of 3:1 as solvent.

Results and discussion

Physicochemical properties of doped $Ni(OH)_2$ precursor and $LiNiO_2$

Scanning electron microscopy (SEM) images of the precursor materials can be seen in Fig. 1. The surface of the precipitated $Ni(OH)_2$precursor materials seem to consist of small primary flakes that have agglomerated into larger secondary particles during precipitation. These observations are analogous to the proposed mechanism for the formation of NCM hydroxides in the presence of aqueous ammonia. During nucleation, a certain fraction of the formed nanometer-sized hydroxide particles is redissolved as metal-ammonium complexes, which in turn will recrystallize from the solution onto the surfaces of the undissolved particles present in the solution. These primary particles will continue to grow into platelet-like shapes until a certain threshold size is reached, after which they agglomerate into larger secondary particles. These secondary particles will further continue to increase in size and become spherical via similar complex formation, dissolution, and crystallization mechanisms, where fresh material is deposited on the surfaces of the secondary particles [25–28].

From Table 1, we can see the lithiated materials have a relatively homogeneous average volumetric particle size distribution and tap density (T.de), except for sample LNO-Cr2-670–5. The somewhat large decrease in

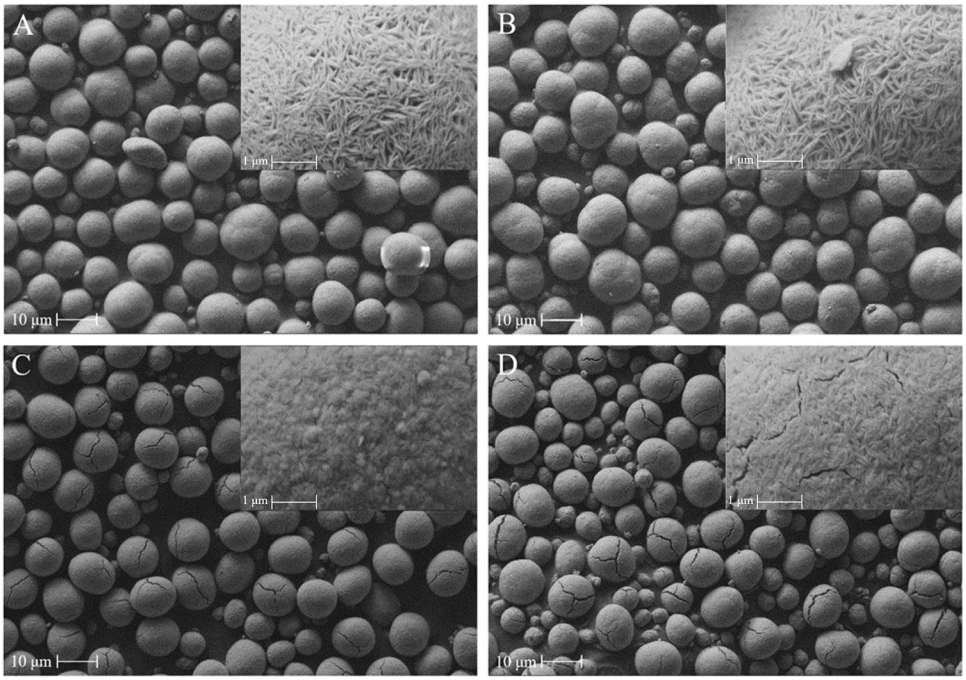

Fig. 1 Selected SEM images of the doped $Ni(OH)_2$ precursor material at 2500 and 50,000 (inset) magnification. **A** Mg-doped precursor (1 mol%), **B** Mg-doped precursor (2 mol%), **C** Mg- and Cr-doped precursor (1 mol% each), and **D** Cr-doped precursor (2 mol%)

tap density in the case of LNO-Cr2-670–5 could be due to increased secondary particle microcracking, visible in Figs. 1D and 2F, yielding less dense particles overall. Furthermore, a closer visual inspection of the surface structure of the chromium-doped materials in Fig. 1C and D would indicate reduced primary particle length, reduced grain boundary size of the primary particles, and denser agglomeration. For the lithiated samples, LNO-670–5 and LNO-Mgx-670–5 materials in Fig. 2A to D show larger primary crystallites on the surface structure as well as reduced secondary particle cracking. The previously mentioned visual observations are further confirmed by the XRD measurements visible in Table 3, which show an increased average crystallite size of the LNO-670–5 and LNO-Mg-670–5 materials, when compared to LNO-Mg1Cr1-670–5 and LNO-Cr2-670–5 [29].

As proposed by Li et al. [23], chromium can be enriched on the particle surface of the NCM material after lithiation.

Table 1 Volumetric particle size distribution and tap density results for the unwashed, lithiated materials

Sample	PSD			T.de
	D10 µm	D50 µm	D90 µm	g/ml
LNO-670–5	6.08	10.5	18.4	2.37
LNO-Mg1-670–5	7.35	11.2	17.1	2.37
LNO-Mg2-670–5	7.31	10.8	15.8	2.40
LNO-Mg3-670–5	7.22	10.8	16.2	2.36
LNO-Mg1Cr1-670–5	7.02	10.1	14.5	2.33
LNO-Cr2-670–5	6.80	10.6	16.5	2.04

A similar mechanism could be an explanation of why the secondary particle growth rates of the Cr-doped materials are significantly impeded during precipitation experiments. It is proposed that chromium is co-precipitated with nickel hydroxide on the surfaces of the primary particles as a separate species, whereby it hinders the growth and agglomeration of the primary particles and thus the formation of secondary particles. The possible presence of individual chromium hydroxide particles between and on the primary particles of the material could yield less mechanically stable material. This in turn could lead to increased microcracking, as the microcracking phenomenon seems to be more prevalent in chromium-containing materials, especially in sample P-LNO-Cr2 with a higher chromium content. Similar behavior can be seen in Fig. 2F, where even after lithiation, the secondary particles show cracking-induced separation and deviation from a spherical shape through the splitting of the secondary particles. This hypothesis is further explored in Chapter 3.2, where the precursor and cathode materials were further analyzed with an electron probe micro-analyzer (EPMA).

As the materials are lithiated with excess lithium precursor to ensure fully lithiated materials, the formation of residual lithium species, such as Li_2CO_3 and LiOH, on the surfaces of the particles is to be expected [29] (Table 2). It has been proposed that NCM-type materials can react readily with CO_2 and H_2O if exposed to air and moisture [30–35]. These surface lithium species are generally thought to consist of lithium carbonate and lithium hydroxide species [31–35]. Additionally, the formation of an Ni carbonate and hydroxide-containing species have also been reported [30, 32]. Even if

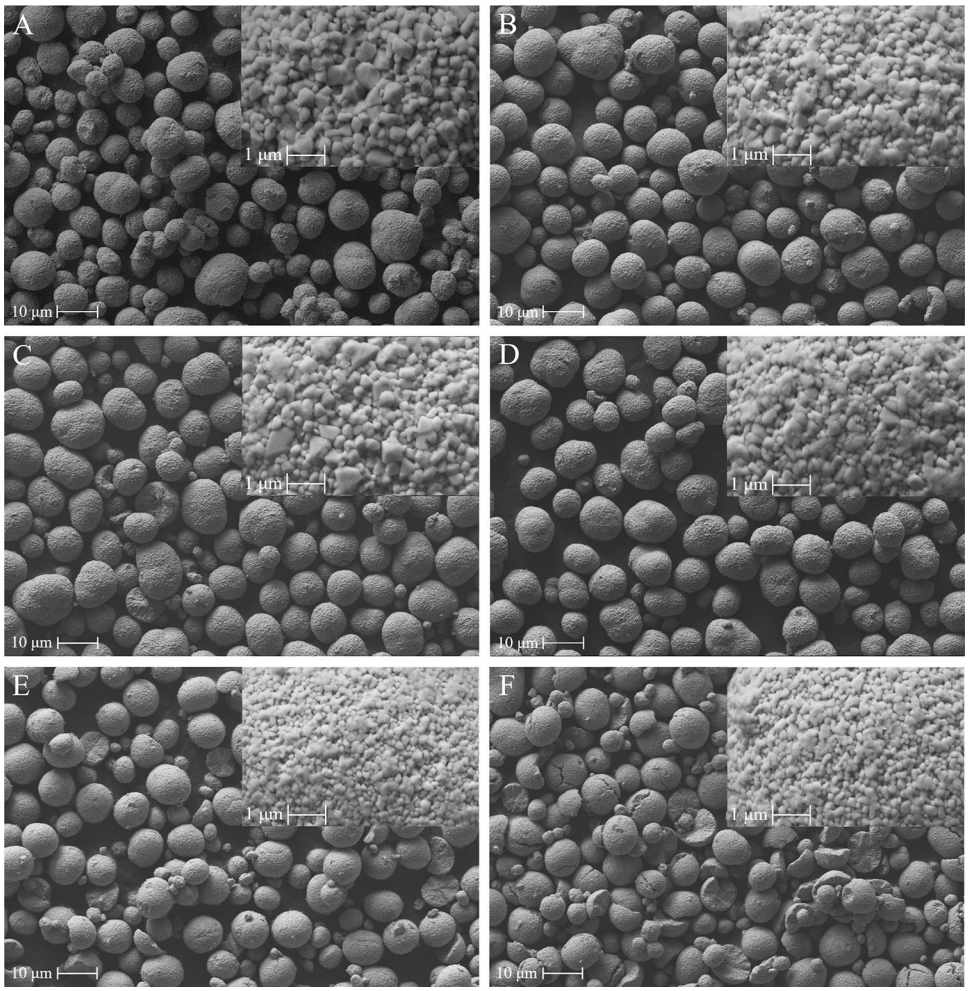

Fig. 2 SEM images of the lithiated materials at 2500 and 50,000 (inset) magnification. **A** LNO-670–5, **B** LNO-Mg1-670–5, **C** LNO-Mg2-670–5, **D** LNO-Mg3-670–5, **E** LNO-Mg1Cr1-670–5, and **F** LNO-Cr2-670–5

the individual roles of residual species and the reaction pathways are a matter of some debate, it is generally accepted that the residual impurity species on the surface of the material facilitate gas formation through side reactions [31, 32, 36, 37] or direct oxidation of Li_2CO_3 [38]. Gaseous compounds will build up within the cell, causing swelling [37] and the formation of electrolyte decomposition products through parasitic side reactions, which hinder lithium diffusion [31, 32].

Table 2 Element ratios measured by ICP-OES, residual lithium content, and BET surface area

Sample	Li/Me	Mg	Cr	Residual Li wt%	BET m^2/g
LNO-670–5	1.08			0.60	
LNO-670–5-WD	0.99			0.08	
LNO-Mg1-670–5	1.15	0.01		0.60	
LNO-Mg1-690–10-WD	1.01	0.01		0.11	1.33
LNO-Mg2-670–5	1.14	0.02		0.56	
LNO-Mg2-670–5-WD	1.01	0.02		0.14	0.96
LNO-Mg2-690–10-WD	0.98	0.02		0.10	
LNO-Mg1Cr1-670–5	1.09	0.01	0.01		
LNO-Mg1Cr1-670–5-WD	0.98	0.01	0.001		
LNO-Cr2-670–5	1.07		0.02		
LNO-Cr2-670–5-WD	0.97		0.002		
LNO-Mg3-670–5	1.13	0.03		0.59	
LNO-Mg3-690–10-WD	1.04	0.03		0.07	1.1

Washing has been proposed as an effective means of removing these residual species, as Li_2CO_3 and LiOH are readily soluble in water [35, 39]; however, prolonged aqueous processing leads to the deterioration of material properties [40] and electrochemical performance [41]. During the washing process, excess removal of Li from the surface structure can occur through an ion-exchange reaction between Li^+ and H^+, which in turn will cause a lithium deficient LNO structure, hindering lithium kinetics, and leading to higher resistance and diminished rate performance [42]. Additionally, the formation of NiO, NiOOH, and $Ni(OH)_2$ after water treatment has been reported in the literature [43]. NiO formation on the surface structure, along with decreased mechanical integrity, was thought to be the main contributing factor in decreased electrochemical performance [40].

The reason for deteriorated electrochemical performance could lie in limited cycling of the cathode materials by the researchers, as less than 200 charge–discharge cycles may be insufficient to fully illustrate the role of gas formation and other parasitic reactions during long-term cell operation. Furthermore, the extended exposure to water might cause significant lithium dissolution, leading to decreased electrochemical performance [40, 41], as rapid washing has been reported to significantly improve the long-term cycling capacity of pure LNO material [4].

Washing of the lithiated materials was attempted in this study. However, during washing, the formation of yellow leachate indicative of chromium dissolution was observed. It is believed that during the lithiation procedure, chromium hydroxide is oxidized and then washed away as a separate phase of lithium chromate, as a change in the liquid's color to orange can be observed after sulfuric acid addition, forming a dichromate ion indicative of Cr^{6+} [44]. ICP results (Table 2) confirm these observations, as the chromium content of the lithiated materials was significantly reduced after washing. Similar behavior of chromium-containing layered chromium-manganese material was observed by Ko et al. [20]. Where the formation of Li_2CrO_4 was observed during lithiation, and successively partly removed by the washing procedure. These observations are further supported by Jones et al. [44], who concluded that nickel- and chromium-containing materials will not form $LiCr_yNi_{1-y}O_2$ at temperatures below 800 °C, but instead will, depending on the starting materials and temperatures, form various separate phases of lithium chromate and lithium nickelate.

As the dissolution of chromium from the material would yield a significantly lower dopant concentration, unwashed materials were employed in successive analyses and electrochemical testing for samples LNO-Mg1Cr1 and LNO-Cr2. Residual lithium analyses were only done for LNO- and Mg-doped samples for the reason mentioned previously. Washing the materials significantly reduces the residual lithium content from approximately 0.6 to 0.1 wt%, as can be seen from Table 2.

Residual lithium titrations results show relatively similar values for the unwashed materials, when compared to the values reported by Xie et al. [11], but much lower values than those reported by Li et al. [10] (Li_2CO_3 13 750 ppm and LiOH 15 620 ppm).

The initial lithiation temperature and time were chosen based on our previous article by Välikangas et al. [4], where 670 °C and 5 h yielded the best electrochemical performance for pure LNO. Additionally, for P-LNO-Mg2, material lithiation temperatures of 650 °C and 690 °C were tested along with a longer lithiation time of 10 h. Washing these materials lithiated at various temperatures and for various periods of time was additionally explored.

Characterization of the material structure with EPMA

The composition of the precursor particle structure was further explored by EPMA, and the analyses are visible in Fig. 3. EPMA analyses were carried out for chromium- and magnesium-containing precursor materials P-LNO-Mg2, P-LNO-Mg1Cr1, and P-LNO-Cr2, as well as for all of the lithiated samples. For each sample, two separate analyses were performed from particles cast in resin, which were then polished for analyses showing the cross-sectional area of the secondary particle.

In the "Physicochemical properties of doped Ni(OH)2 precursor and LiNiO2" section, the hypothesis that chromium would be separately precipitated on the surfaces of the primary particles, thus influencing particle growth kinetics during precipitation, was proposed. EPMA results show, perhaps, slightly different reasons for particle cracking. In some cases, chromium and magnesium can separately form concentrated areas inside the secondary particle of the hydroxide precursor material (Fig. 3D, E, F, and H). Both dopant materials facilitate the formation of a slightly hollow core region, visible in the SEM images (Fig. 3A, B, and C). This concentrated core formation can be simply explained by the differing complexation behaviors, as nickel will readily form a soluble nickel-ammine complex with ammonia, while Mg and Cr will not at a lower initial pH range, as suggested by the Medusa-Hydra calculations. It is proposed that Mg and Cr will be preferentially precipitated as seed particles unto which nickel hydroxide forms. However, when a concentrated chromium core is present, there seems to be a visible crack emanating from the core to the outer surface region of the particle, while magnesium-doped material seems to be less influenced by the core accumulation. For both chromium-containing precursor materials, particle cracking seems to be extensive, even with no visible concentrated chromium core. One rational explanation for this may lie in the sample preparation and polishing procedure, as not all of the visible particles are necessarily cross-sectionally cut from the center line forming two equal hemispheres,

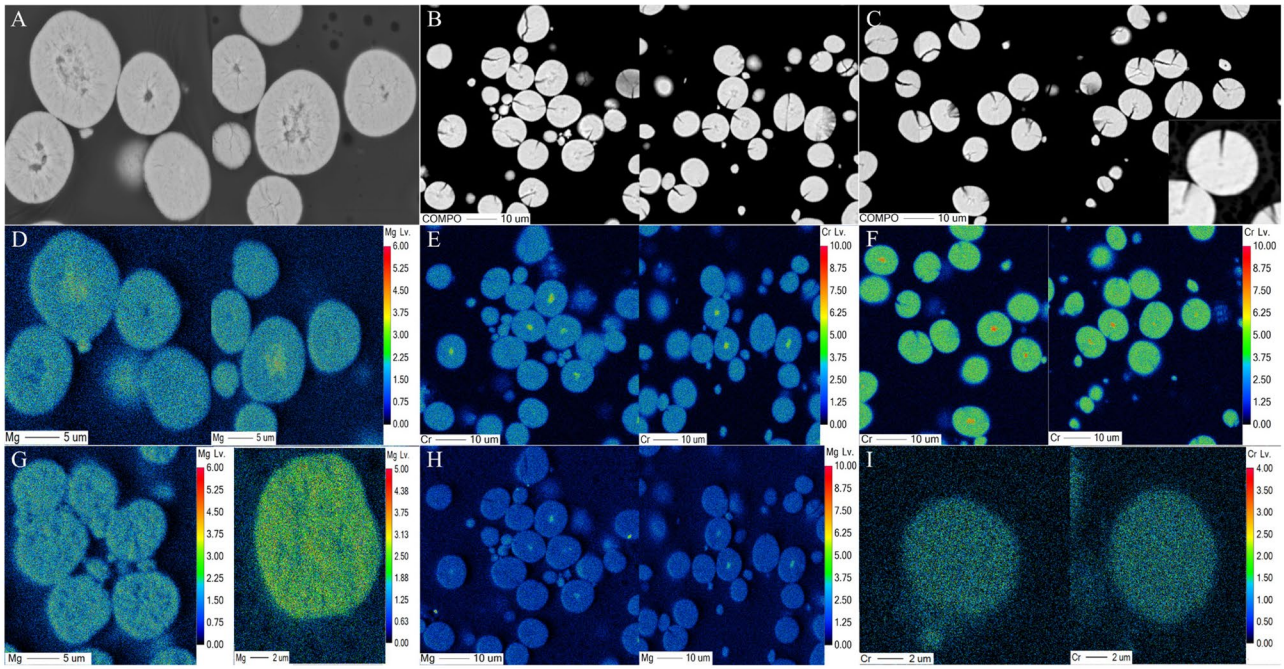

Fig. 3 EPMA analyses of the precursor materials. **A** Cross-section SEM image of P-LNO-Mg2, **B** cross-section SEM image of P-LNO-Mg1Cr1, **C** cross-section SEM image of P-LNO-Cr2, **D** EPMA determination of P-LNO-Mg2 magnesium content, **E** EPMA determination of P-LNO-Mg1Cr1 chromium content, **F** EPMA determination of P-LNO-Cr2 chromium content, **G** EPMA determination of LNO-Mg2 magnesium content (left: LNO-Mg2-670-5UW and right: LNO-Mg2-690-10WD), **H** EPMA determination of P-LNO-Mg1Cr1 magnesium content, and **I** EPMA determination of LNO-Cr2 chromium content

showing not the inside of the sphere, but a plane section of the particle.

For the lithiated samples, both magnesium and chromium seem to be rather evenly spread out within the particle (Fig. 3G and I), possibly indicating ordering and movement of the dopants during lithiation procedure. No visible enrichment of chromium on the particle surfaces was observed after lithiation, as proposed by Li et al. [23].

XRD and Rietveld refinement results

Two sets of XRD-based analyses were carried out. XRD for all the samples, as well as synchrotron hard X-ray measurements for the doped samples, were utilized to accurately study the physical properties of the samples. Table 3 shows the XRD parameters for the lithiated samples. In our previous article, it was demonstrated that stoichiometrically phase pure LNO material can be prepared, when given the right synthesis conditions, with minimal cation mixing below 1.3% [4]. For the unwashed samples, few trends can be seen as the *c*-axis parameter seems to increase as Mg content increases. Similarly, the *c*/*a* value increases, stabilizing at an Mg content of 2 mol%. It was proposed by Murali et al. [53] that a non-linear development of *c*/*a* can be observed as a function of Mg doping.

Lithiation temperature seems to influence both crystallite sizes *a* and *c* of the LNO-Mg2 washed material. Crystallite size *a* increases as temperature and time increases. A similar trend can be seen for crystallite size *c*, except for sample LNO-Mg2-670-10WD. Additionally, the same sample has a significantly lower 003/104 integrated intensity ratio when compared to other Mg-containing samples. It has been proposed by Ohzuku et al. [45] that an integrated intensity ratio of 003/104 can be used as an indication of electrochemical performance. As it is descriptive of inter-mixing between Ni^{3+} and Li^{+}, lower intensity ratios would signify a reduced electrochemical performance of the material.

Figure 4 shows the integrated 1D SXRD patterns and intensity (arb. unit) vs. 2 theta angles for LNO samples with different dopants. The data shown here were normalized to 1 using "I/max(I) (I: intensity)" without background subtractions. All the samples show a single-phase, layered $LiCoO_2$ structure with an *R*-3 *m* space group. As seen from the magnified views of some diffraction peaks in the right panel of Fig. 4, a left shifting of the diffraction peaks is distinguishable due to Cr doping, while an increase in Mg dopant induces minor deviations. Figure 4B also highlights the doublet peak splitting of (018)/(110), (021)/(10 10), (00 12)/(02 14), and (01 11)/(205) in Mg-doped LNO. On the contrary, these splitting peaks were seen to

Table 3 XRD parameters for all samples

Sample	*a*-axis (Å)	*c*-axis (Å)	*c/a*	*c/3a*	(003)/(104) Int.I	crystallite size *a* (Å)	crystallite size *c* (Å)
LNO-670–5	2.87579	14.1910	4.9346	1.6449	1.346	2170.69	2797.88
LNO-670–5-WD	2.87613	14.1947	4.9353	1.6451	1.343	2054.64	2680.64
LNO-Mg1-670–5	2.87460	14.1909	4.9367	1.6456	1.339	1764.08	2439.11
LNO-Mg1-690–10-WD	2.87386	14.1911	4.9380	1.6460	1.372	3560.60	5648.35
LNO-Mg2-670–5	2.87456	14.1946	4.9380	1.6460	1.342	2598.18	3735.13
LNO-Mg2-670–5-WD	2.87347	14.1997	4.9416	1.6472	1.341	2668.58	3962.92
LNO-Mg2-650–10-WD	2.87756	14.2081	4.9376	1.6459	1.320	933.74	1358.99
LNO-Mg2-670–10-WD	2.87626	14.2040	4.9384	1.6461	1.289	2950.84	3127.43
LNO-Mg2-690–10-WD	2.87434	14.1966	4.9391	1.6464	1.341	3336.42	4450.59
LNO-Mg3-670–5	2.87493	14.1963	4.9380	1.6460	1.337	2398.16	3480.04
LNO-Mg3-690–10-WD	2.87583	14.2010	4.9381	1.6460	1.380	2653.18	4104.98
LNO-Mg1Cr1-670–5	2.87868	14.1993	4.9326	1.6442	1.314	1371.04	1590.77
LNO-Cr2-670–5	2.88057	14.2000	4.9296	1.6432	1.271	1293.48	1449.54

have mainly asymmetric peak shapes in Cr-doped LNO. Some minor peaks (marked by * in Fig. 4B) not belonging to the *R*-3 *m* space group are also visible especially in 2 at. % Cr-doped LNO sample. This might reveal the presence of an impurity phase in the samples. However, the intensity is quite low, 1/500 to the strongest (003) peak of LNO, indicating that this impurity can be ignored. Thus, we assume that all the Mg and Cr atoms are successfully incorporated into an R-3 m LNO lattice.

SXRD patterns of all the samples were analyzed by Rietveld refinement method. The refinement results are shown in Fig S1 (supplement). The unit-cell parameters are summarized in Table 4. It can be seen that both the *a*, *c* lattice parameters and *c/a* ratios of LNO increase with increases in Mg content. This small deviation might suggest that disorder of the hexagonal crystal structure remains, compared to a 4.93627 from undistorted LNO structure (*R*-3 *m* symmetry with cell parameters of $a = 2.87772$ Å, $c = 14.20520$ Å, ICDD PDF 00–066-0856). The addition of Cr dopant, on the contrary, reduces *c/a* ratios. I_{003}/I_{104} decreases due to Mg and Cr doping, perhaps suggesting that the cation disorder increases.

For atomic occupancy, we assumed that Li ions occupy the 3a site; Ni and Cr take the 3b site, O is located in the 6c site, and Mg is assumed to be located in the Li and/or Ni layers. Table 5 gives the atomic occupancies of all the samples.

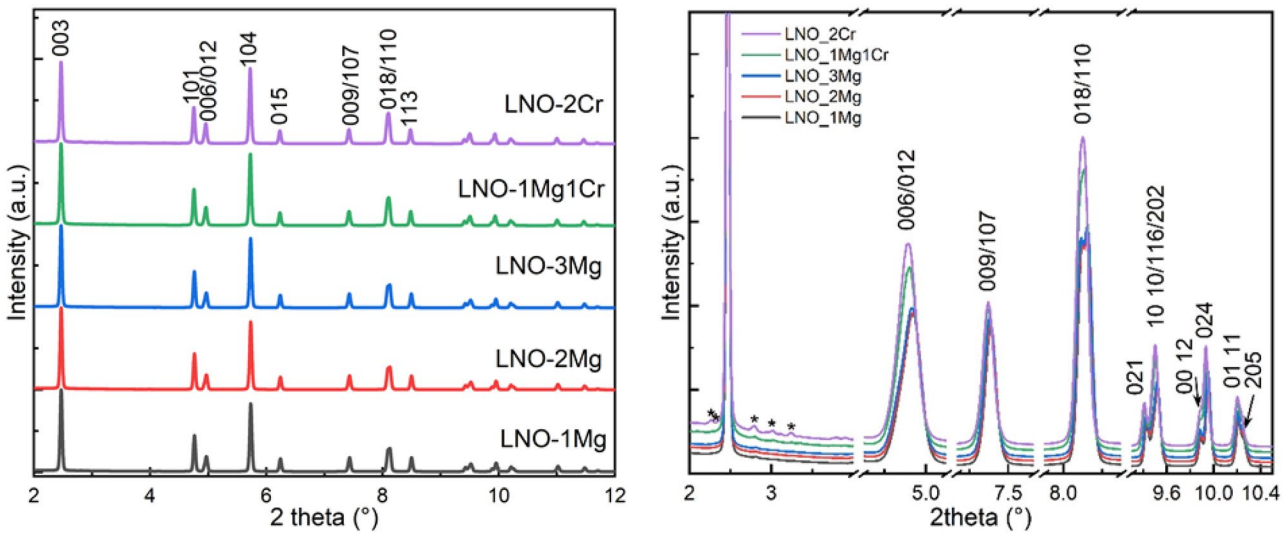

Fig. 4 **A** Synchrotron X-ray diffraction (SXRD) patterns of the LNO samples and **B** magnified view showing the peak splitting and asymmetric peaks due to the diffraction from doublets with a close interplanar distance

Table 4 Rietveld refinement results of SXRD data for LNO samples

Sample	a (Å)	c (Å)	c/a	I_{003}/I_{104}	Size (nm)	R_{wp} (%)	R_p (%)
LNO-Mg1-670–5	2.87403(4)	14.1830(2)	4.93492	1.13984	26.0(2)	3.29	2.47
LNO-Mg2-670–5	2.87417(4)	14.1864(2)	4.93582	1.13835	26.1(1)	3.19	2.38
LNO-Mg3-670–5	2.87508(4)	14.1919(2)	4.93617	1.12830	26.2(2)	3.35	2.50
LNO-Mg1Cr1-670–5	2.87892(5)	14.1929(3)	4.92994	1.09364	24.4(1)	5.73	3.85
LNO-Cr2-670–5	2.88034(6)	14.1926(3)	4.92740	1.05509	24.4(1)	3.23	2.41

Occupancy of Mg is predominantly in the Li sites, which is highly ascribed to the smaller ionic radius of Mg^{2+} (0.72 Å) as compared with 0.76 Å of Li^+. Part of the Mg atoms were observed migrating to Ni sites in Table 5 due to an addition in excess of 3 at.%, which is consistent with observations made by Pouillerie et al. [9], where an increase of Mg doping to over 2 at% leads to a binominal distribution of Mg in both the Li and Ni layers. Interestingly, these findings would suggest an upper limit of the amount of magnesium that can be utilized as a pillar dopant in the Li layer (Fig. 5).

Consistent with the SXRD study, similar plots for X-ray PDF data of all samples are observed in Fig. 6A. The PDF pattern simulated using the aforementioned $LiNiO_2$ structure (R-3 m symmetry with cell parameters of $a = 2.87772$ Å, $c = 14.20520$ Å, ICDD PDF 00–066-0856) is very close to the experimental profiles. In general, peaks below 1.8 Å are termination ripples that do not represent any real structural features. The first peak at 2.09 Å in the simulated profiles is ascribed to the M–O atomic pairs in [MO_6] octahedron. This peak position shifts to smaller r s around 1.96 Å due to the

Table 5 Atomic occupancy obtained from Rietveld refinement of the SXRD data for LNO samples with a space group of R-3 m

Sample	Atom	Site	x	y	z	Occu.
LNO-Mg1-670–5	Li1	3a	0	0	0	0.982(1)
	Ni1	3a	0	0	0	0.008(1)
	Mg1	3a	0	0	0	0.010(1)
	Ni2	3b	0	0	1/2	1.000
	Mg2	3b	0	0	1/2	0
	O	6c	0	0	0.24137(4)	1.000
LNO-Mg2-670–5	Li1	3a	0	0	0	0.975(1)
	Ni1	3a	0	0	0	0.005(1)
	Mg1	3a	0	0	0	0.020(1)
	Ni2	3b	0	0	1/2	1.000
	Mg2	3b	0	0	1/2	0
	O	6c	0	0	0.24136(4)	1.000
LNO-Mg3-670–5	Li1	3a	0	0	0	0.970(1)
	Ni1	3a	0	0	0	0.005(1)
	Mg1	3a	0	0	0	0.025(1)
	Ni2	3b	0	0	1/2	0.995(2)
	Mg2	3b	0	0	1/2	0.005(2)
	O	6c	0	0	0.24139(4)	1.000
LNO-Mg1Cr1-670–5	Li1	3a	0	0	0	0.980(2)
	Ni1	3a	0	0	0	0.010(2)
	Mg1	3a	0	0	0	0.010(2)
	Ni2	3b	0	0	1/2	0.990(5)
	Mg2	3b	0	0	1/2	0.000(5)
	Cr1	3b	0	0	1/2	0.010(5)
	O	6c	0	0	0.24147(4)	1.000
LNO-Cr2-670–5	Li1	3a	0	0	0	0.956(1)
	Ni1	3a	0	0	0	0.044(1)
	Ni2	3b	0	0	1/2	0.980(14)
	Cr1	3b	0	0	1/2	0.020(14)
	O	6c	0	0	0.24162(5)	1.000

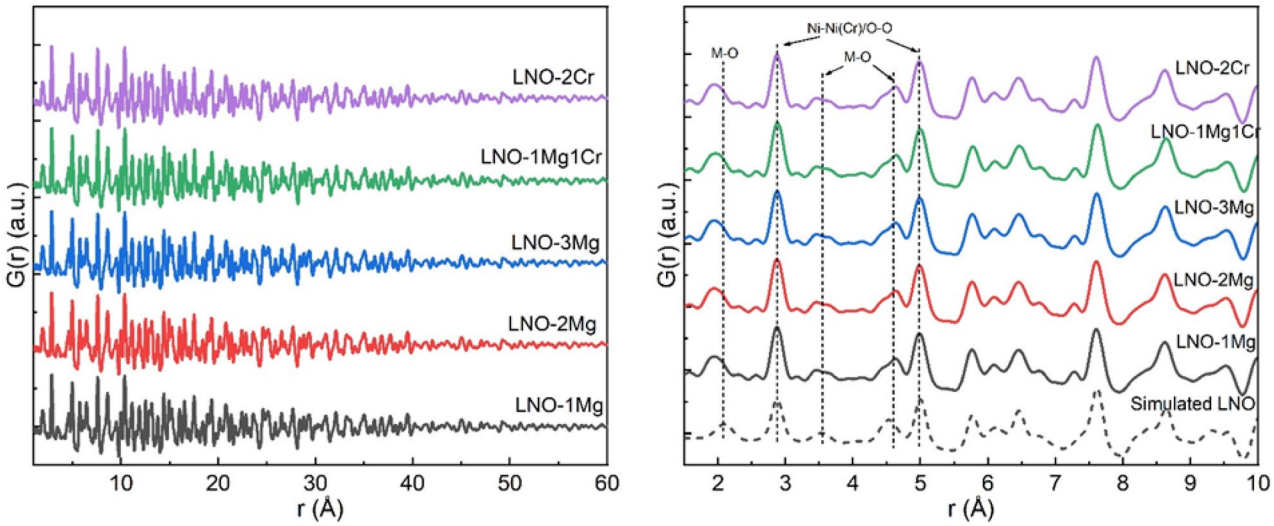

Fig. 5 The atomic PDF pair distribution function G(r) for all the LNO powders

superposition of M–O atomic pairs (M could be Li, Ni, and Mg according to the SXRD results) and smaller Cr–O and Mg(Li site)- O than Ni–O and Li–O distances. The correlation distance in the simulated profile at 2.89 and 5 Å corresponds to the six coordinated Ni–Ni(Cr) bonds along the NiO_2 layer or O–O neighboring distances, which occurs in all of the experimental data. Peaks above 5 Å are due to the superposition of multiple structural features and are therefore not straightforward to assign. It should be noted that the PDF peaks for experimental LNOs that were assigned to M–O pairs are seen to have asymmetrical multiple peak features, which is reported to be possibly associated with elongated [NiO_6] octahedra due to local Jahn–Teller distortions [47, 48]. Such results indicate that the local lattice Jahn–Teller distortion of Mg - and Cr - doped LNO samples fabricated by this method is highly oriented.

Electrochemical performance

Coin cell testing data can be seen in Table 6 that shows first charge capacity with tap charge, DC to 3.0 V, DC to 2.6 V with tap charge, Coulombic efficiency, DC after 62 cycles, and capacity retention after 62 cycles. Magnesium - doped LNO material performs extraordinarily well, when compared to the chromium - doped ones, which suffer from limited capacity retention after 62 cycles, even when compared to the pristine LNO. The unwashed LNO - Mg - containing materials have slightly lower initial charges and discharge capacities when compared to pure LNO, but a higher capacity retention. After 62 cycles, the capacity of the LNO - Mg samples was between 199.6 and 190.6 mAh / g, which is slightly higher in some cases than pristine LNO - 670–5 at 193.6 mAh / g and significantly higher than that of LNO - Mg1Cr1 - 670–5 151.0 mAh / g and LNO - Cr2 - 670–5 138.2 mAh / g. The capacity retention of the Cr materials seems to fade faster initially the more chromium is present in the material. Similar behavior is observed in pouch cells, where the capacity retention of unwashed samples fades significantly faster as chromium content is increased (Fig. 7E). As the cycling behavior of LNO - Mg2 - 670–5 proved to be effective, additional Mg - doped samples with similar physicochemical characteristics were tested in electrochemical cells and further analyzed as seen previously. These testing results can be seen in Figs. 6, 7, and 8.

Rate performance of the unwashed materials as well as washed materials LNO - Mg2 - 670 - 5WD and LNO - 670 - 5WD can be seen in Table 7.

Figure 7B shows the first cycle - specific capacity and capacity retention after 62 cycles of the unwashed Mg - containing materials as a function of Mg content in coin cells. Blue, orange, and gray lines represent charge and discharge capacities on the left axis. Yellow line in Fig. 7B represents capacity retention after 62 cycles, visible on the right side of the figure. As the magnesium content increases, the specific capacity decreases nearly linearly. This behavior could be explained by Mg positioning itself on lithium sites, since for every one Mg atom, two lithium atoms are excluded from the structure [49]. However, as Mg content increases from 0 to 3 mol %, so does capacity retention, significantly, from 87.6 to 100 % after 62 cycles.

Lithiation temperatures influence on electrochemical performance was tested for washed LNO - Mg2 material as well as to LNO - Mg3. From Fig. 7C, the sample lithiated at a temperature of 650 °C performs the worst, while very little difference exists between materials lithiated

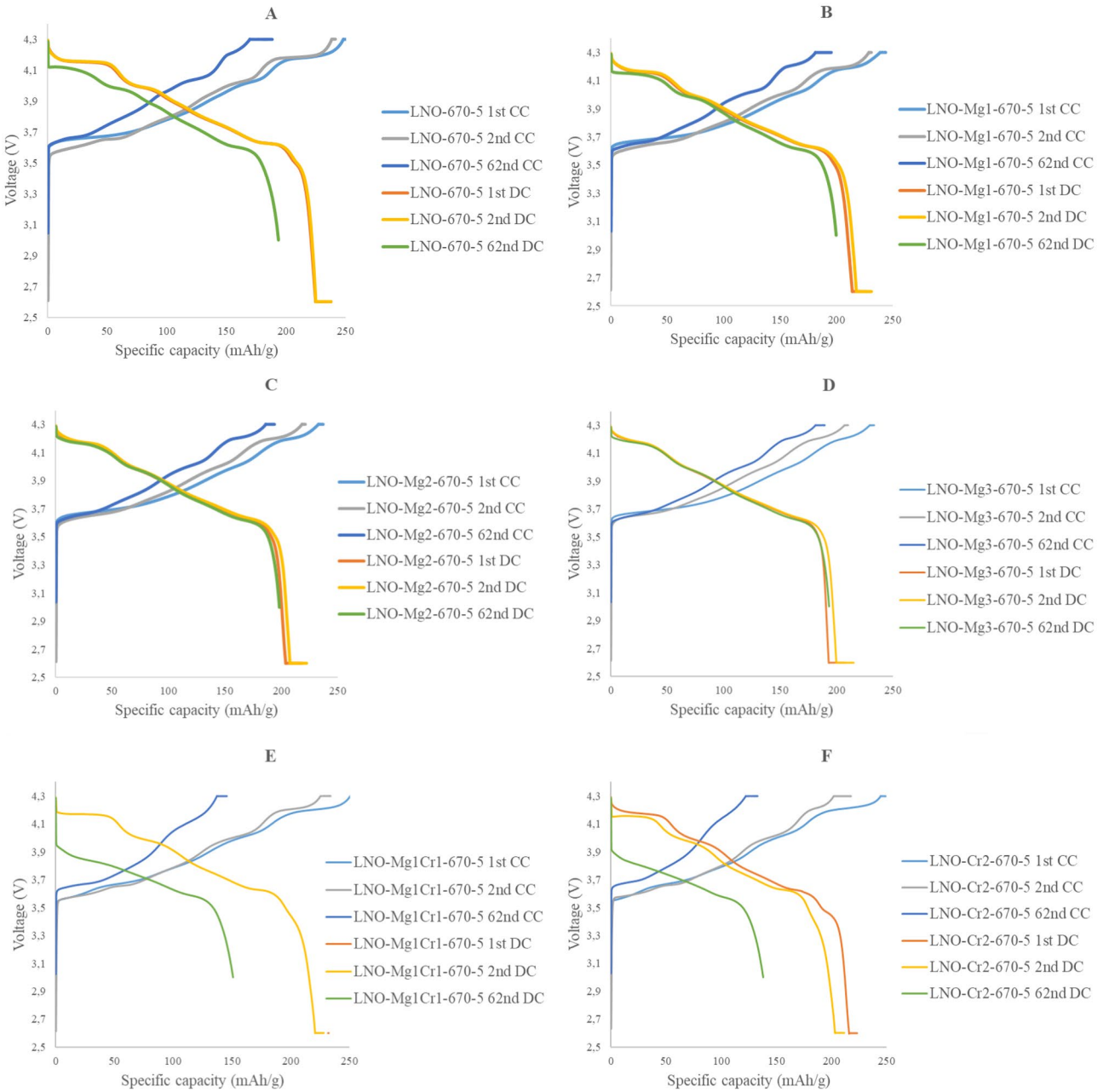

Fig. 6 First, second, and 62nd charge and discharge curves for unwashed samples. **A** LNO - 670–5, **B** LNO - Mg1 - 670–5, **C** LNO - Mg2 - 670–5, **D** LNO - Mg3 - 670–5, **E** LNO - Mg1Cr1 - 670–5, and **F** LNO - Cr2 - 670–5

Table 6 Coin cell cycle performance and capacity retention after 62 cycles

Sample	Charge 4.3 V 0.1 C + 0.015 C (1st)	DC 3.0 V 0.1 C (1st)	DC 2.6 V 0.1 C (1st)	Coulom. eff 3.0v (1st) 0.1 C	Coulom. eff 2.6 v (1st) 0.1 C	DC 3.0 V 0,1 C (62)	Retention after 62 cycles
	mAh/g	mAh/g	mAh/g	%	%	mAh/g	%
LNO - 670–5	251.6	221.1	237.9	87.9	94.5	193.6	87.6
LNO - Mg1 - 670–5	243.4	209.8	228.0	86.2	93.7	199.6	95.2
LNO - Mg2 - 670–5	237.4	200.6	218.3	84.5	91.9	198.3	98.9
LNO - Mg3 - 670–5	233.1	190.6	207.0	81.8	88.8	190.6	100.0
LNO - Mg1Cr1 - 670–5	254.1	221.5	232.4	87.2	91.5	151.0	68.2
LNO - Cr2 - 670–5	249.4	212.2	223.5	85.1	89.6	138.2	65.1

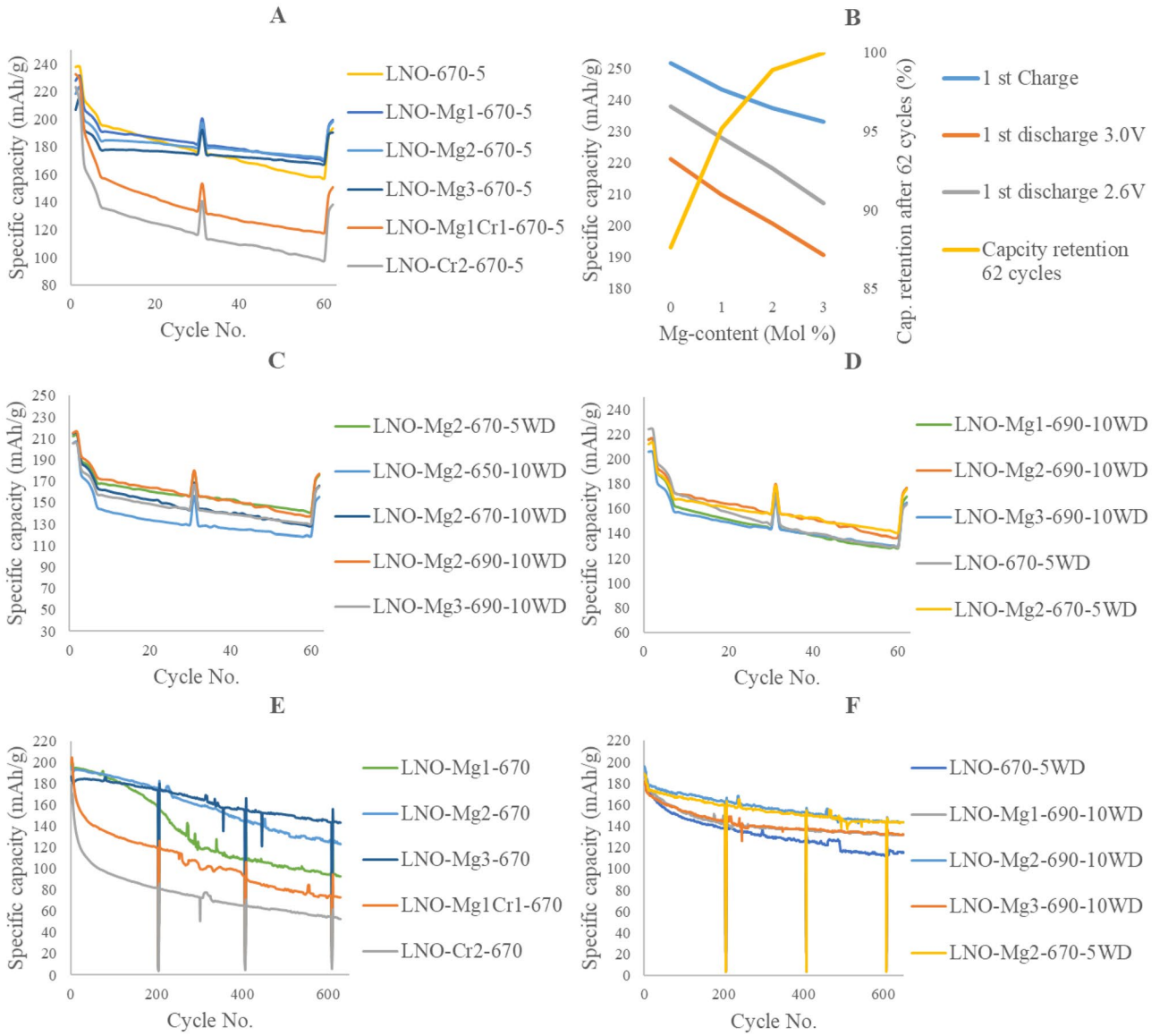

Fig. 7 Coin and pouch cell testing data. **A** Coin cell results of unwashed samples, **B** coin cell results as a function of Mg content, **C** coin cell results of washed samples, **D** coin cell results of washed samples at different temperatures, **E** pouch cell results of unwashed samples, and **F** pouch cell results of the washed samples

at 670 °C for 5 h and 690 °C for 10 h in a coin cell and after 500 cycles in a pouch cell, when tested after washing. However, LNO - Mg2 - 690 - 10WD has a somewhat higher initial capacity of 196.2 mAh / g in comparison with LNO - Mg2 - 670 - 5WD's capacity of 188.4 mAh / g. Interestingly, material lithiated at 670 °C for 10 h has limited electrochemical performance, somewhat deviating from the trend. It is believed that this material did not lithiate fully, as similar behavior can be seen in the pouch cell (data not shown here). This is further confirmed by XRD analyses (Table 3), which show a significantly smaller integrated intensity ratio 003 / 104 value, which deviates from the trend of the other Mg - containing materials and, as mentioned before, is proposed to affect electrochemical performance due cation disorder [46].

The difference between the electrochemical behavior of the washed and unwashed material can be seen in Fig. 7. For the unwashed pouch cells, after a prolonged testing of 600 cycles, material containing 3 mol % of Mg has the highest discharge capacity of 150.3 mAh / g at 0.5 C rate cycled between 2.5 and 4.2 V (Fig. 7E). However, for the washed samples, material containing 2 mol % has the highest capacity after 600 cycles in both coin and pouch cells (Fig. 7D and F). It was proposed by Palacín et al. [42] that in NCM - type materials lithium dissolution increases as BET surface area increases, forming lithium

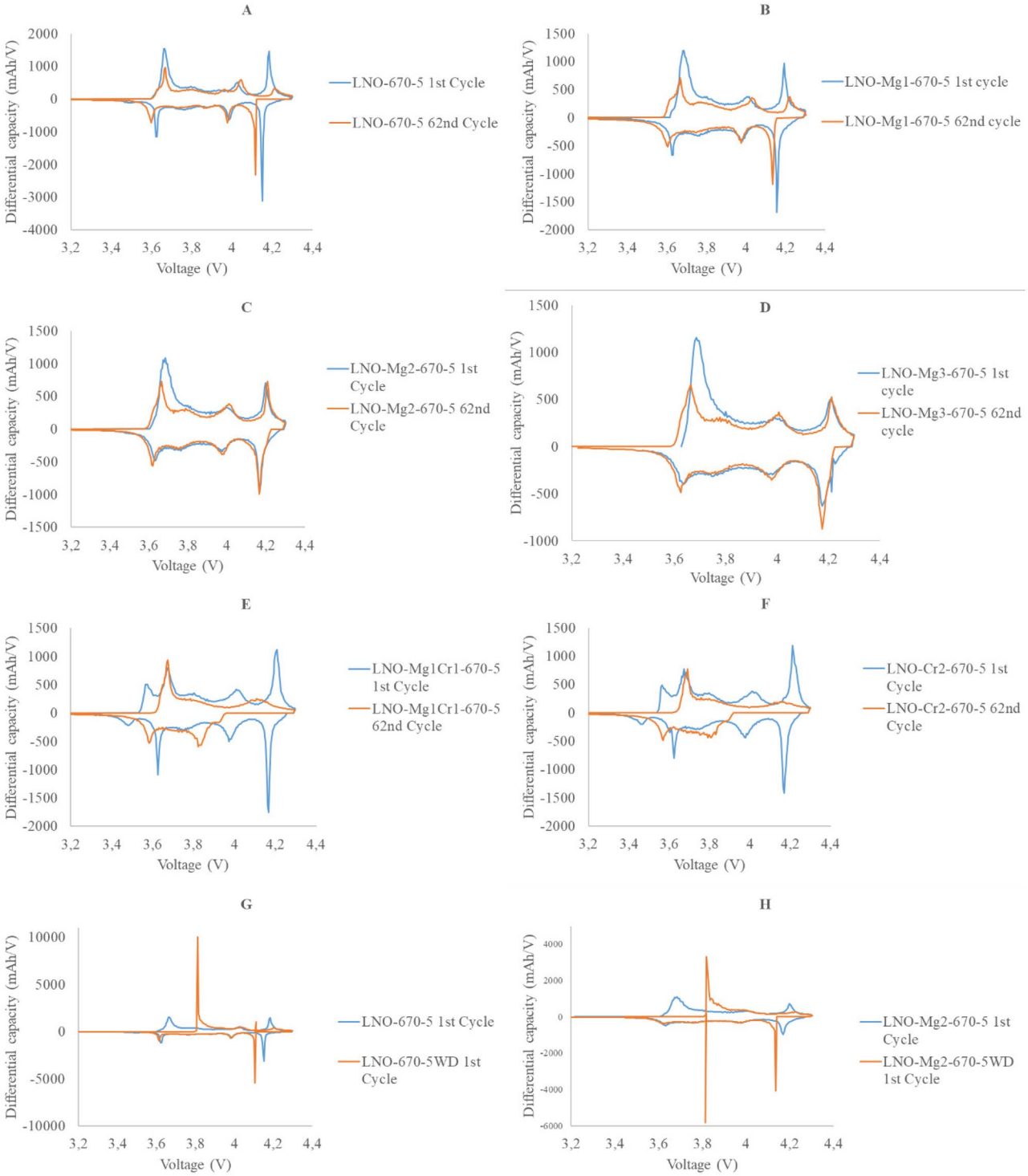

Fig. 8 Differential capacity measurements of the prepared materials. **A** LNO-670–5, **B** LNO-Mg1-670–5, **C** LNO-Mg2-670–5, **D** LNO-Mg3-670–5, **E** LNO-Mg1Cr1-670–5, **F** LNO-Cr2-670–5, **G** LNO-670-5WD and LNO-670–5, and **H** LNO-Mg2-670-5WD and LNO-Mg2-670–5

deficient phases. From Table 2, LNO-Mg2-690-10WD has the lowest surface area of the washed Mg-containing samples. Furthermore, the amount of larger macropores in sample LNO-Mg2-670-5WD (> 50 nm) is lower than 47.4 % in comparison to 55.6–58 % for the samples LNO-Mg1-690-10WD and LNO-Mg3-690-10WD,

Table 7 Coin cell rate performance for selected samples

Sample	Discharge 4.3–3.0 V						
	0.1 C (1st)	0.1 C (2nd)	0.2 C (3rd)	0.3 C (4th)	0.5 C (5th)	1 C (6th)	2 C (7th)
	mAh / g	mAh / g	mAh / g	mAh / g	mAh / g	mAh / g	mAh / g
LNO - 670–5	221.1	221.9	215.0	210.5	206.9	203.0	196.4
LNO - Mg1 - 670–5	209.8	213.9	208.1	204.4	201.8	197.3	191.4
LNO - Mg2 - 670–5	200.6	204.5	200.1	197.2	194.5	190.3	184.5
LNO - Mg3 - 670–5	190.6	196.5	193.1	190.4	188.5	183.9	178.0
LNO - Mg1Cr1 - 670–5	221.5	215.6	192.7	182.7	174.9	167.1	158.4
LNO - Cr2 - 670–5	212.2	197.9	167.5	159.4	153.6	145.9	136.7
LNO - 670 - 5WD	203.2	204.3	197.8	193.9	190.4	184.4	173.2
LNO - Mg2 - 670 - 5WD	193.0	195.0	189.4	186.6	183.4	177.6	168.0

respectively. Higher macropore and BET surface area could cause differences in washing behavior, which in turn could lead to increased Li dissolution and surface species change, thus explaining the difference in electrochemical performance between the washed and unwashed Mg - doped samples. Additional comparisons can be made between samples LNO - Mg2 - 670–5 and LNO - Mg2 - 670 - 5WD. The washed material outperforms the unwashed after 362 cycles. After 500 cycles, the unwashed material delivers a capacity of 133.8 mAh/g in comparison to 145.1 mAh/g for the washed. Similarly, the sample LNO - Mg2 - 670 - 5WD outperforms LNO - 670 - 5WD in the coin and pouch cells, indicative of the beneficial influence of magnesium on capacity retention. However, as washing reduces the initial capacities and rate performance of the tested materials, as can be seen in Table 7, as well as having a possible influence on performance based on physical properties, further research is needed to optimize washing procedures and methods. It is further proposed that additional heat treatment of the material after washing might be beneficial and restore some of the lost capacity by the reformation of the surface LNO crystal structure.

Differential capacity measurements can be seen in Fig. 8. During the first charge (the upper region in Fig. 8), the material undergoes a phase transformation from a hexagonal 1 (H1) phase to a monoclinic phase (M) after 3.6 V, which can be seen as the peak in the differential capacity measurements. A second, and larger, charge peak occurs when the material further changes from monoclinic to hexagonal 2, and finally, the last peak corresponds to the phase change from hexagonal 2 (H2) to hexagonal 3 (H3). The lower region of the figure shows the associated discharge curve, where the phase changes occur inversely [50, 51]. However, in the case of chromium - doped samples, there appears to be one additional peak at around 3.5 V (Fig. 8E and F). Furthermore, for the chromium - doped samples, the complete disappearance of any redox peaks before 3.9 V, associated with the initial phase changes during discharge after 62 cycles can be seen.

In the case of pure LNO and the magnesium - doped samples, these peaks are clearly visible and seem to dissipate and decrease in intensity, especially in the H2–H3 and H3–H2 regions, as the amount of Mg increases. This would indicate smoother phase changes being facilitated by the magnesium, which are also visible in Fig. 6, as they exhibit smoother discharge and charge curves indicative of easier phase transformations and reversibility of the phase, as proposed by Li et al. [10] and Xie et al. [11].

To further explore the poor electrochemical performance of Cr - containing materials, P - LNO - Mg1 material was lithiated with chromium hydroxide to test the influence of microcracking, as it has been reported to significantly influence capacity retention for NCM - type materials [52]. Even though the desired composition of Cr was slightly lower than the desired 1 mol % (0.7 mol %), material displayed reduced electrochemical performance after 62 cycles, when compared to the pristine LNO - Mg1 material. Therefore, it is believed that microcracking of the lithiated material is not the main reason for the diminished electrochemical performance of the chromium - containing materials. However an extensive microcracking of the precursors (Fig. 1C and D) and the lithiated products (Fig. 2E and F) can be seen from SEM images. It is possible that the structural integrity of the materials is compromised by the chromium doping. This would lead to a possible diminution of the cathode material during cycling. The anisotropic expansion and contraction could have a larger impact on the chromium - doped materials, as decreased mechanical integrity could lead to breakage of the secondary particle, thus exposing fresh surface area sensitive to electrolyte reactions.

SXRD patterns suggest the presence of an impurity phase not belonging to the *R*-3 *m* space group. Even though rather minor, it is suspected that this could be one of the reasons

for the reduced electrochemical performance of the chromium-doped materials. Chromium might not form a solid solution with lithium nickelate at the tested lithiation temperature. A separate phase of lithium chromate is formed as a result of the lithiation procedure, as we were able to wash away hexavalent lithium chromate. These observations support the findings of Jones et al. [44], where they were able to synthesize single-phase solid solution chromium-containing materials at reasonable temperatures only in conjunction with cobalt. Furthermore, these findings might explain the findings of Li et al. [23], where partial incorporation of chromium into cobalt-containing material (NCM811) was observed. Interestingly Mohan et al. [22] were able to synthesize $LiCr_{0.1}0Ni_{0.9}O_2$ via a sol–gel method at 800 °C. If so, these findings might suggest that chromium doping for pure LNO has little practical value [53], as the required high lithiation temperatures could impede electrochemical performance via the conversion of space groups *R*3*m* to *Fm*-3 *m* as rock salt structure (NiO) [46]. This suggests that additional considerations, such as sufficient lithiation temperatures for various dopants, should be included when doping NCM-type materials.

From Fig. 8E and F, the additional redox peak at 3.5 V, visible in the Cr-doped samples, dissipates after successive cycling, finally disappearing all together after 62 cycles. Furthermore, Cr-doped samples show fairly high initial charge capacities; see Table 6. Few suggestions are put forth as to what could be the mechanistic explanation for the reduced capacity retention and electrochemical performance of chromium-doped materials. SXRD-data and Rietveld refinement suggest that the amount of Ni in the lithium layer increases for the Cr-doped samples, when compared to the Mg-containing samples. This could be due to the charge compensation of the crystal lattice, as Cr^{6+} would be compensated by the increase of divalent nickel, which would then enter the lithium layer during lithiation[23].It was proposed by Poullier et al. [9] that cation mixing would significantly impede lithium diffusion and deintercalation. During electrochemical cycling, Ni^{2+} would be oxidized to Ni^{3+}, reducing the distance of NiO_2 layers in the structure as well as influencing the neighboring Ni atoms in the hexagonal structure. These influences would lead to increases in cell polarization and reversible capacity loss.

It was proposed by Lee et al. [52] and Li et al. [50] that hexavalent chromium can migrate to octahedral lithium sites during cycling, due to their similar ionic sizes. Chromium atoms will block lithium pathways, thus hindering lithium de/intercalation movement and significantly contributing to capacity decay. Furthermore, the redox reaction of chromium is highly irreversible and does not necessarily undergo a change of 3^+ to 6^+, but 3^+ to 4^+ only partly in $LiCrO_2$ [55]. Incorporation of chromium into the LNO structure could cause significant capacity deterioration rather quickly, as visible in Fig. 7A. Therefore, it is believed that the main reason for chromium caused capacity deterioration is its detrimental influence on lithium diffusion kinetics, either by facilitating the cation mixing of nickel or by migrating to lithium sites during cycling. If a separate phase of lithium chromate is formed on the surface of the material, it could behave like the mechanism proposed by Lyu et al. [54], where chromium in $LiCrO_2$ material will migrate to Li sites and undergoes highly irreversible oxidation from 3^+ to 4^+, thus having limited reversible capacities and possibly hindering lithium kinetics on the surface of the bulk material. As mentioned before, the disappearance of the initial discharge redox peaks after 62 cycles could further give indication that chromium has entered the lithium site and as to why the capacity has deteriorated drastically that chromium has entered the lithium site and the capacity has deteriorated drastically. This leads to only partial oxidation and electrochemical inactivity.. This blocking effect could block the phase changes and intercalation of lithium into the material and thus drastically influence capacity, as the H3-H2 phase transition has a large contribution to the specific capacity of the cathode material and as can be seen from the specific capacities of the Cr-doped materials after cycling.

To summarize the potential sources of reduced electrochemical performance of the Cr - doped material, visible microcracking of the precipitated and lithiated material can be seen. This could have some influence on the electrochemical performance and capacity retention, as mechanically instable particles could break to smaller particles exposing fresh surface area to electrolyte reactions and causing reduced contact with electrode. A possible twofold mechanism is proposed based on visual observations of washing as well as XRD analysis. The main mechanism is thought to involve the irreversibility of chromium redox reaction. A formation of lithium chromate as a separate phase could possibly block lithium intercalation reactions on the surfaces of the secondary particles after successive cycling as electrochemically inert layer could be formed on the surfaces. If however chromium is fully incorporated to the LNO structure the reported migration of Cr^{6+} into Li sites could hinder lithium intercalation reactions, via previously mentioned mechanism, where Cr would not fully undergo redox reactions, but form a blocking component that hinders Li kinetics.

It has been proposed that for olivine type structures, the positioning of magnesium doping has a significant influence on the capacity and Li-ion diffusion of the material due to magnesium-induced blocking effects in the lithium layer [56]. It is postulated here that in addition of previously mentioned pillaring effect magnesium doping of layered *R*3*m*material, Mg effectively blocks cation mixing between Li and Ni, as indicated by Rietveld refinement. In our case, magnesium mostly lies in the lithium layer that could effectively hinder lithium ion diffusion. However as cation mixing is

diminished by Mg positioning, these effects could prove to be overall beneficial as electrochemically inert magnesium does not undergo previously mentioned redox cycle of nickel in the lithium layer that is taught to cause local shrinkage, thus compromising electrochemical performance [9]. Furthermore, magnesium ions can migrate during electrochemical cycling [56, 57]; however, as reported by Choi et al. [56], for type materials after first cycle, their position is fixed in the lithium layer for successive cycles possibly further diminishing cycling introducing cation mixing for this type of materials.

A comparison of differential capacity measurements between washed and unwashed materials can be seen in Fig. 8G and H. Of particular note is the drastic increase of the first phase change associated with H - M1 in the charge cycle for the washed material when compared with the unwashed. It was proposed by Li et al. [50] and Rougier et al. [57] that the phase change of H1 - M is indicative of slow lithium diffusion due to kinetic hindrance especially prevalent in lithium deficient phases [57]. These observations could explain the reduced capacities of the washed materials. Washing not only removes the residual lithium species but lithium from the surface structure as well, creating a varied combination of Li -, Ni -, and O - containing materials, deviating from stoichiometrically pure crystalline LNO structure, as proposed by Palacin et al. [42] and Toma et al. [41]. Furthermore, washing - induced detrimental effects could be especially pronounced in cobalt - free materials [43]. It is further proposed that an after treatment method might prove to be beneficial in order to reduce washing - induced detrimental influences. Additional brief thermal treatment after washing could restore the surface structure and restore the some of the initial capacities lost after washing.

Conclusions

The aim of this research was to test out the hypothetical synergistic influences of Mg and Cr doping on the electrochemical properties of cathode materials prepared by a simple two - step co - precipitation and lithiation procedure. During the precipitation procedure, both magnesium and chromium form a concentrated core particle unto which nickel hydroxide precipitates. During lithiation, the elements in question will migrate from the core and spread evenly in the secondary particle. Chromium - containing materials display relatively limited electrochemical performance and rapid capacity fading when combined with LNO, while purely Mg - doped samples perform excellently due to phase stabilizing effects. However, there seems to be an upper limit for Mg positioning into the lithium layer, as it was observed partly located in the nickel layer, as suggested by Rietveld refinement.

Washing of pure or high nickel - containing materials proves to be challenging. While it can be used to improve capacity after prolonged testing, there is probably an inevitable loss of lithium from the surface structure due to a cation - exchange reaction between Li^+ and H^+. Slight differences in surface area and handling procedures could cause a significant formation of lithium - deficient phases, which limit lithium diffusion, as suggested by differential capacity measurements. After treatment procedure of the washed materials, it could prove to be beneficial in restoring the surface structure and mitigate washing - induced initial capacity losses. Further research is needed to mitigate the effects of washing as residual lithium species, if left on the material surface, negatively impact on the capacity rather quickly.

Based on visual observations, SXRD - data and Rietveld refinement, two possible sources are proposed for the diminished electrochemical performance of Cr - containing materials. The rather minor impurity phase present in the XRD data and the formation of yellow leachate during washing could be indicative of the formation of separate phases of LNO and lithium chromate. However, if Cr is fully incorporated into the LNO structure and into the nickel site, the highly irreversible redox reaction of chromium could block lithium pathways. In both cases, this highly irreversible redox reaction of hexavalent chromium is believed to be the main reason for the capacity decay and poor electrochemical performance of Cr - doped materials.

Supplementary Information The online version contains supplementary material available at https://doi.org/10.1007/s10008-023-05652-1.

Acknowledgements M.Sc. Marcin Selent, Centre for Material Analysis, University of Oulu, is acknowledged for the help with XRD analysis. Part of the research described in this paper was performed at the Canadian Light Source, a national research facility of the University of Saskatchewan, which is supported by the Canada Foundation for Innovation (CFI), the Natural Sciences and Engineering Research Council (NSERC), the National Research Council (NRC), the Canadian Institutes of Health Research (CIHR), the Government of Saskatchewan, and the University of Saskatchewan.

Funding Open Access funding provided by University of Oulu including Oulu University Hospital. This research was funded by Business Finland, grant number (University of Oulu, BATCircle2.0, No. 44612/31/2020).

Declarations

Conflict of interest The authors declare no competing interests.

Open Access This article is licensed under a Creative Commons Attribution 4.0 International License, which permits use, sharing, adaptation, distribution and reproduction in any medium or format, as long as you give appropriate credit to the original author(s) and the source, provide a link to the Creative Commons licence, and indicate if changes were made. The images or other third party material in this article are included in the article's Creative Commons licence, unless indicated otherwise in a credit line to the material. If material is not included in the article's Creative Commons licence and your intended use is not

permitted by statutory regulation or exceeds the permitted use, you will need to obtain permission directly from the copyright holder. To view a copy of this licence, visit http://creativecommons.org/licenses/by/4.0/.

References

1. Gallo M, Marinelli M (2020) Sustainability 12(18):7499
2. Li W, Ericson EM, Manthiram A (2020) Nat Energy 5(1): 2058–7546
3. Delmas C. MeÂneÂtrier M, Croguennec L, Saadoune I, Rougier A, Pouillerie C, Pradoa G, GruÈne M, FourneÁs L (1999) Electrochim Acta 45:243–253
4. Välikangas J, Laine P, Hietaniemi M, Hu T, Tynjälä P, Lassi U (2020) Appl Sci 10:8988
5. Yoon CS, Jun D - W, Myung S - T, Sun Y - K (2017) ACS Energy Lett 2:1150–1155
6. Dixit M, Markovsky B, Schipper F, Aurbach D, Major DT (2017) J Phys Chem C 121(41):22628–22636
7. Manthiram A, Knight JC, Myung S - T, Adv S - M (2016) Energy Mater 6:1501010
8. Bianchinia M, Roca - Ayatsa M, Hartmann P, Brezesinski T, Janek Angew J (2019) Chem Int Ed Engl 58(31):10434–10458
9. Pouillerie C, Croguennec L, Biensan Ph, Willmann P, Delmas C (2000) J Electrochem Soc 147:2061–2069
10. Li H, Zhou P, Liu F, Li H (2019) F. Cheng J. Chen. Chem Sci 10:1374–1379
11. Xie Q, Li W, Manthiram A (2019) Chem Mater 31:938–946
12. Muto S, Tatsumi K, Kojima Y, Oka H, Kondo H, Horibuchi K, Ukyo Y (2012) J Power Sources 205:449–455
13. Xiang J, Chang C, Zhang F, Sun J (2009) J Alloys Compd 475:483–487
14. Chowdari BVR, Subba Rao GV (2001) Solid State Ion 140:55–62
15. Mu L, Zhang R, Kan WH, Zhang Y, Li L, Kuai C, Zydlewski B, Rahman MM, Sun C - J, Sainio S, Avdeev M, Nordlund D, Xin HL, Lin F (2019) Chem Mater 31(23):9769–9776
16. Gao Y, Yakovleva MV, Ebner WB (1998) Electrochem solid - state lett 1(3):117–119
17. Mu L, Kan WH, Kuai C, Yang Z, Li L, Sun C - J, Sainio S, Avdeev M, Nordlund D, Lin F (2020) ACS Appl. Mater Interfaces 12(11):12874–12882
18. Seong WM, Manthiram A (2020) ACS Appl. Mater Interfaces 12(39):43653–43664
19. Yoshida T, Maezono R, Hongo K (2020) ACS Omega 5(22):13403–13408
20. Koa YN, Kima JH, Leea J - K, Kanga YC, Lee J - H (2012) Electrochim Acta 69:345–350
21. Mangani IR, Park CW, Kim SH, Kim J (2005) Ionics 11:366–369
22. Mohan P, Kumar KA, Kalaignan GP, Muralidharan VS (2012) J Solid State Electrochem 16:3695–3702
23. Jun Li L, Wang ZX, Liua QC, Yea C, Chena ZY, Gonga L (2012) Electrochim Acta 77:89–96
24. Toby BH, Von Dreele RB (2013) J Appl Cryst 46:544–549
25. van Bommel A, Dahn JR (2009) Chem Mater 21:1500–1503
26. Barai P, Feng Z, Kondo H, Srinivasan V (2019) J Phys Chem B 123:3291−3303
27. Mei - xun P, Xiang - qian S (2007) J Cent South Univ Technol 14:310–314
28. Arai H, Okada S, Ohtsuka H, Ichimura M, Yamaki J (1995) Solid State Ion 80(3–4):261–269
29. Sicklinger J, Metzger M, Beyer H, Pritzl D, Gasteiger HA (2019) J Electrochem Soc 166:A2322
30. Faenza NV, Bruce L, Lebens - Higgins ZW, Plitz I, Pereira N, Piper LFJ, Amatuccia GG (2017) J Electrochem Soc 164:A3727
31. Jung R, Morasch R, Karayaylali P, Phillips K (2018) J Electrochem Soc 165(2):A132
32. Matsumoto K, Kuzuo R, Takeya K, Yamanaka A (1999) J Power Sources 81–82:558–561
33. Zhuang GV, Chen G, Shim J, Song X, Ross PN, Richardson TJ (2004) J Power Sources 134(2):293–297
34. Kim J, Hong Y, Ryu KS, Kim MG, Cho J (2006) Electrochem solid - state lett 9(1):A19 - A23
35. Metzger M, Strehle B, Solchenbach S, Gasteiger HA (2016) J Electrochem Soc 163(2):A132
36. Kim Y (2013) J Mater Sci 48:8547–8551
37. Renfrew SE, McCloskey BD (2017) J Am Chem Soc 139: 17853–17860
38. Xiong X, Wang Z, Yue P, Guo H, Wu F, Wang J, Li X (2013) J Power Sources 222:318–325
39. Azhari L, Zhou X, Sousa B, Yang Z, Gao G, Wang Y (2020) ACS Appl Mater Interfaces 12(52):57963–57974
40. Pritzl D, Teufl T, Freiberg ATS, Strehle B, Sicklinger J, Sommer H, Hartmann P, Gasteiger HA (2019) J Electrochem Soc 166:A4056
41. Toma T, Maezono R, Hongo K (2020) ACS Appl. Energy Mater 3(4):4078–4087
42. Palacin MR, Larcher D, Audemer A, Sac-Épée N, Amatucci GG, Tarascon J - M (1997) Low-Temperature Synthesis of LiNiO2: Reaction Mechanism, Stability, and Electrochemical Properties. J Electrochem Soc 144(12):4226–4236. https://doi.org/10.1149/1.1838171
43. Laitinen R, Toivonen J (2007) Yleinen ja epäorgaaninen kemia, Hakapaino Oy. Otatieto, Gaudeamus Helsinki University Press, Helsinki
44. Jones CDW, Rossen E, Dahn JR (1994) Solid State Ion 68:65–69
45. Ohzuku T, Ueda A, Nagayama M, Iwakoshi Y, Komori H (1993) Electrochim. Acta 38(9):1159–1167
46. Chung J - H, Proffen Th, Shamoto S, Ghorayeb AM, Croguennec L, Tian W, Sales BC, Jin R, Mandrus D, Egami T (2005) Phys Rev B 71(6):064410
47. Sicolo S, Mock M, Bianchini M, Albe K (2020) Chem Mater 32(23):10096–10103
48. Li H, Cormier M, Zhang N, Inglis J, Li J, Dahn JR (2019) J Electrochem Soc 166:A429
49. de Biasi L, Schiele A, Roca - Ayats M, Garcia G, Brezesinski T, Hartmann P, Janek J (2019) Chemsuschem 12(10):2240–2250
50. Li H, Zhang N, Li J, Dahn JR (2018) J Electrochem Soc 165:A2985–A2993
51. Lim J - M, Hwang T, Kim D, Park M - S, Cho K, Cho M (2017) Sci Rep 7:39669
52. Lee E, Park JS, Wu T, Sun C - J, Kim H, Stair PC, Lu J, Zhou D, Johnsona CS (2015) J Mater Chem A 3:9915–9924
53. Murali N, Vijaya Babu K, Ephraim Babu K, Veeraiah V (2015) Chem Sci Trans 4(4):1031–1036
54. Lyu Y, Ben L, Sun Y, Tang D, Xu K, Gu L, Xiao R, Li H, Chen L, Huang X (2015) J Power Sources 273:1218–1225
55. Ni J, Zhao Y, Chen J, Gao L, Lu L (2014) Electrochem commun 44:4–7
56. Choi A, Lim J, Kim H - J, Jung SC, Lim H - W, Kim H, Kwon M - S, Han YK, Oh SM, Lee KT (2018) Adv Energy Mater 8(11):1702514
57. Rougier A, Gravereau P, Delmas C (1996) J Electrochem Soc 143(4):1168–1175

Publisher's Note Springer Nature remains neutral with regard to jurisdictional claims in published maps and institutional affiliations.